



City Research Online

City St George's, University of London

Citation: Zeng, Q., Gonzalez-Avila, S. R., Dijkink, R., Koukouvinis, P., Gavaises, M. & Ohl, C-D. (2018). Wall shear stress from jetting cavitation bubbles. *Journal of Fluid Mechanics*, 846, pp. 341-355. doi: 10.1017/jfm.2018.286

This is the accepted version of the paper.

This version of the publication may differ from the final published version. To cite this item please consult the publisher's version.

Permanent repository link: <https://openaccess.city.ac.uk/id/eprint/20073/>

Link to published version: <https://doi.org/10.1017/jfm.2018.286>

Copyright and Reuse: Copyright and Moral Rights remain with the author(s) and/or copyright holders. Copies of full items can be used for personal research or study, educational, or not-for-profit purposes without prior permission or charge, unless otherwise indicated, provided that the authors, title and full bibliographic details are credited, a hyperlink and/or URL is given for the original metadata page and the content is not changed in any way. For full details of reuse please refer to [City Research Online policy](#).

Wall Shear Stress from Jetting Cavitation Bubbles

Qingyun Zeng¹, Silvestre Roberto Gonzalez-Avila¹, Rory Dijkink²,
Phoevos Koukouvini³, Manolis Gavaises³ and Claus-Dieter Ohl^{1,4†}

¹Division of Physics and Applied Physics, School of Physical and Mathematical Sciences,
Nanyang Technological University, 21 Nanyang Link, Singapore 637371

²Academie of Life Science, Engineering & Design at the Saxion University of Applied Sciences,
M.H. Tromplaan 28, 7513AB Enschede, The Netherlands

³City University London, Northampton Square, London EC1V 0HB, United Kingdom

⁴Institute of Experimental Physics, Otto von Guericke University Magdeburg, D-39016
Magdeburg, Germany

(Received xx; revised xx; accepted xx)

The collapse of a cavitation bubble near a rigid boundary induces a high-speed transient jet accelerating liquid onto the boundary. The shear flow produced by this event has many applications, examples are surface cleaning, cell membrane poration, and enhanced cooling. Yet the magnitude and spatio-temporal distribution of the wall shear stress are not well understood, neither experimentally nor by simulations. Here we solve the flow in the boundary layer using an axisymmetric compressible Volume of Fluid (VOF) solver from the OpenFOAM framework and discuss the resulting wall shear stress generated for a non-dimensional distance, $\gamma = 1.0$ ($\gamma = h/R_{max}$, where h is the distance of the initial bubble centre to the boundary, R_{max} the maximum spherical equivalent radius of the bubble). The calculation of the wall shear stress is found reliable once the flow region with constant shear rate in the boundary layer is determined. Very high wall shear stresses of 100 kPa are found during the early spreading of the jet followed by complex flows composed of annular stagnation rings and secondary vortices. Although the simulated bubble dynamics agrees very well with experiments we obtain only qualitative agreement with experiments due to inherent experimental challenges.

1. Introduction

Cavitation bubbles expanding and shrinking near rigid boundaries move towards the boundary due to the action of the secondary Bjerknes force (Blake & Gibson 1987; Best & Kucera 1992). The oscillating flow near the wall creates naturally a strong and unsteady boundary layer flow with high shear rates. Additionally, the radial flow is accompanied by a jetting flow accelerating liquid to impinge on and spread along the wall.

Historically, the shear stress generated from steady impinging jets on solid walls has been solved by Glauert (1956), and confirmed through simulations (Deshpande & Vaishnav 1982; Phares *et al.* 2000), and experiments (Narayanan *et al.* 2004; Visser *et al.* 2015). However, the shear stress produced by transient jets from near wall cavitation has recently received more attention, in particular for its importance for surface cleaning (Ohl *et al.* 2006a; Kim *et al.* 2009; Gonzalez-Avila *et al.* 2011) and cell membrane poration cells (Ohl *et al.* 2006b; Le Gac *et al.* 2007). Very few experiments have tried to measure the wall shear stress. Dijkink & Ohl (2008) combined high-speed photography with a hot film

† Email address for correspondence: claus-dieter.ohl@ovgu.de

anemometer and found short peaks with stress amplitudes of up to 3.5 kPa occurring right after the jet impact. Given the limited temporal bandwidth of their device the maximum shear stress reported may only be a lower bound. Their sensor can only measure at a single location. Thus, to map spatial stress requires many measurements with identical bubbles, which is difficult to achieve. To fill this knowledge gap, we present here a numerical approach to estimate the wall shear stress. It is based on the Finite Volume method (FVM) to discretize the fluid domain and the Volume of Fluid (VOF) method to capture the bubble-water interface. We can reliably simulate the bubble dynamics through the first and second collapse and obtain a spatio-temporal map of the wall shear stress.

This work is organized as follows; first, we verify the numerical model with experiments and previous shear stress measurement from Dijkink & Ohl (2008); then we study the flow field details near the boundary to clarify the flow features that lead to the wall shear stress. After that a spatio-temporal map of the wall shear stress distribution is presented and discussed. A test of our numerical method against previous works and an analytic solution is provided in the Appendix.

2. Methodology

Here we resolve the shear flow produced by a cavitation bubble collapsing near a solid boundary in water. The flow field is obtained by solving the compressible Navier-Stokes equations and capturing the gas-water interface with the VOF method based on the Finite Volume framework of OpenFOAM (Weller *et al.* 1998). The flow is dominated mostly by inertia of the liquid and the compressibility of the gas; the viscosity is only important close to the surface. For simplicity we model the initial (laser created) cavitation bubble consisting of non-condensable gas starting from a small volume at high pressure. The sharp interface of the cavitation bubble is captured by solving the transport equation for the volume fraction of the liquid (Miller *et al.* 2013; Koch *et al.* 2016):

$$\frac{\partial \alpha}{\partial t} + \nabla \cdot (\alpha \mathbf{u}) + \nabla \cdot (\alpha(1 - \alpha)\mathbf{U}_r) = \alpha(1 - \alpha) \left(\frac{\psi_g}{\rho_g} - \frac{\psi_l}{\rho_l} \right) \frac{Dp}{Dt} + \alpha \nabla \cdot \mathbf{u} \quad , \quad (2.1)$$

where α is the volume fraction of the liquid phase, \mathbf{u} the velocity field, p the pressure. \mathbf{U}_r is the relative velocity between two phases, which helps to ensure a sharp interface (Rusche 2003). Compressibility is included on the right hand side, which contains the compressibility of both phases (liquid and gas) with $\psi = D\rho/Dp$ from the Equation of State (EOS). For the gas phase a polytropic EOS is used while for the liquid phase the Tait EOS (Macdonald 1969) is applied, similar to the cavitation bubble simulations in Koukouvinis *et al.* (2016*a,b*) and Koch *et al.* (2016).

In the compressible NS equations, we use the single-field formulation and treat the two-phases as a compressible and immiscible Newtonian fluid while neglecting the heat and mass transfer.

$$\frac{\partial \rho}{\partial t} + \nabla \cdot (\rho \mathbf{u}) = 0 \quad (2.2)$$

$$\frac{\partial \rho \mathbf{u}}{\partial t} + \nabla \cdot (\rho \mathbf{u} \mathbf{u}) = -\nabla p + \nabla \cdot \mathbf{s} + \mathbf{f}_\delta \quad , \quad (2.3)$$

where ρ is the density of the fluid, \mathbf{s} the viscous stress tensor which is calculated as $\mathbf{s} = \mu(\nabla \mathbf{u} + \nabla \mathbf{u}^T - \frac{2}{3}(\nabla \cdot \mathbf{u})\mathbf{I})$, with the dynamic viscosity μ and the identity tensor \mathbf{I} . \mathbf{f}_δ is the source term due to surface tension which is modeled with the Continuous-Surface-Force (CSF) method (Brackbill *et al.* 1992). Flow properties are calculated based on the

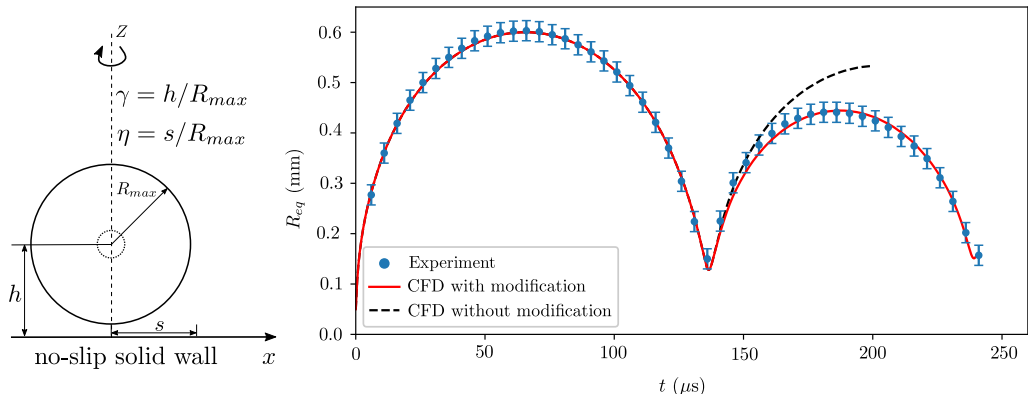


FIGURE 1. (a) Sketch of the problem and parameters. The dashed circle is the bubble nucleation and the solid circle is the bubble at maximum size; (b) Comparison of the equivalent spherical bubble radius from simulations (lines) with the experiment (filled symbols). The dashed line shows the result using a constant polytropic exponent of $\kappa = 1.4$; and the red solid line represents the result using a polytropic exponent of $\kappa = 1.4$ from $t = 0 \mu\text{s}$ to $t = 136.5 \mu\text{s}$ and a higher polytropic exponent of $\kappa_2 = 2.4$ from $t = 136.5 \mu\text{s}$. The error bar presents the uncertainty from the recorded images.

volume fraction of the liquid with $\zeta = \zeta_l \alpha + \zeta_g (1 - \alpha)$, where ζ_l and ζ_g are physical properties of the liquid and the gas.

We verify the numerical method by comparing the simulation results with experiments. In the experiment cavitation bubbles are created with a 6-ns duration pulse from a Q-switched laser (New Wave, $\lambda = 532 \text{ nm}$), which is focused at a distance h close to a wall; the bubble dynamics is recorded with a high-speed camera (Photron SAX-2, Japan) operating at 200,000 fps (293 ns exposure time). The high speed recorded images with pixel size of $20 \mu\text{m}$ are used to validate the gas phase dynamics and thus the flow field in the numerical simulations. For the validation of the wall shear stress from the simulations, we benchmarked the model with earlier simulations of a submerged steady wall jet impinging on a surface Deshpande & Vaishnav (1982), see Appendix. We also compare the simulation result with experiments Dijkink & Ohl (2008) of cavitation bubble induced wall shear stress. To simplify the simulation an axisymmetric domain is chosen; a size of 5 mm in radial and 10 mm in axial directions. The computational mesh contains 101 grid points in radial direction and 201 grid points in axis direction initially. These are refined recursively four times. In the area of interest, i.e. where the bubble is located the cell size is about $3 \mu\text{m}$ wide. For the solid boundary a no-slip condition is used. In the near boundary region, the mesh is further refined recursively down to a spacing $\Delta x = 0.05 \mu\text{m}$, to resolve a linear increasing velocity within the thin boundary layer.

3. Results

3.1. Comparison with Experiments

Before we have a detailed look into the flow near to the boundary and the wall shear stress generated we compare the overall bubble dynamics together with the snapshots of the bubble shape. Figure 1(a) shows the sketch of the problem and introduces the coordinates of the axisymmetric problem. Figure 1 compares the volume equivalent spherical bubble radius between the experiment (filled symbols, $R_{\text{max}} = 0.6 \text{ mm}$, $\gamma = 1.1$) and the simulations (lines). In the simulations and the experiments the bubble due to the high pressure inside expands in the initially stagnant liquid. By adjusting the this

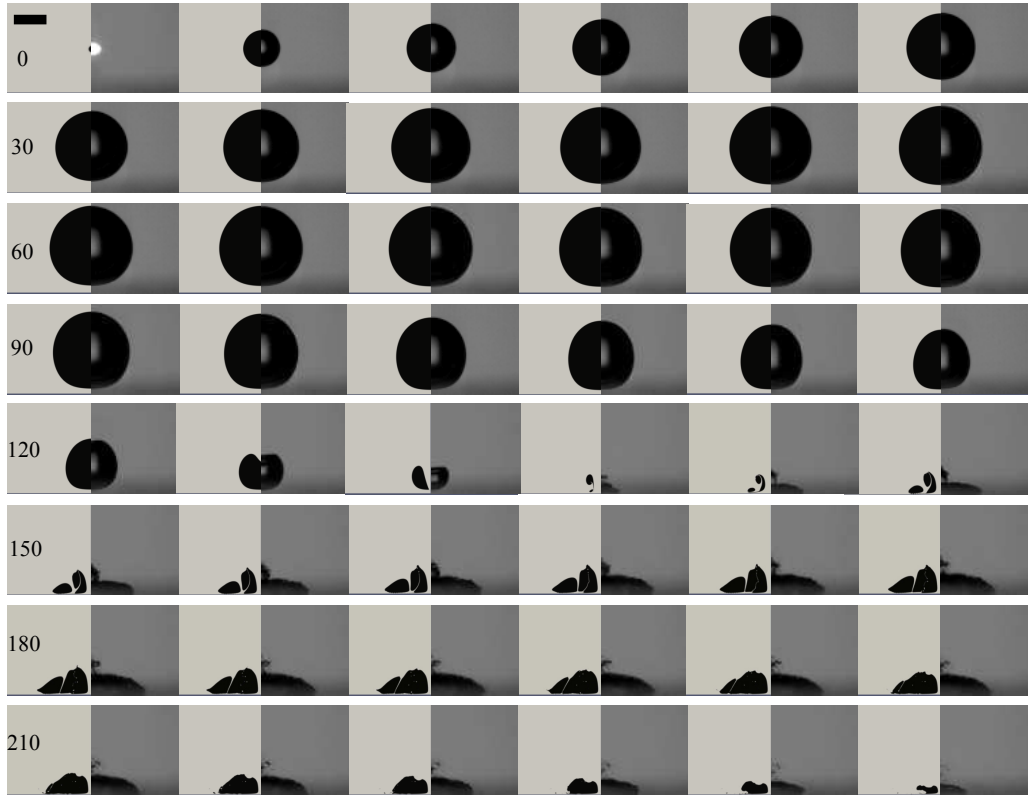


FIGURE 2. Comparison of bubble shape evolution for standoff distance $\gamma = 1.1$. The left part in a single frame is the simulation result, while the right part is the experimental result. Time of the first frame in each row is indicated in μs , inter-frame time is $5 \mu\text{s}$, and the scale bar represents 0.5 mm . The boundary is below each frame.

pressure while keeping the radius, $R(t = 0) = 50 \mu\text{m}$, constant we can achieve good agreement for the expansion stage to an almost spherical bubble and the later shrinkage. Yet, after re-expansion we find a considerable deviation of the equivalent bubble radius between the experiment and a straightforward simulation (dashed line); the bubble after collapse expands much larger in the simulations. We attribute this difference to the cushioning effect of the gas during the collapse: the non-condensable gas slows down the last stage of the collapse resulting in less energy being lost from acoustic radiation and viscous damping, hence allowing for a larger re-expansion. To deal with this discrepancy, while not modeling the mass transfer Lee *et al.* (2007) implemented an experimental correlation accounting for the energy loss during the collapse into their boundary integral method based on data from Cole (1965). Wang (2014) also considered the energy loss due to shock wave emission during the early expansion stage and the late bubble collapse and uses the bubble wall Mach number as a criterion. Both methods achieved reasonable agreement with experimental results, however they are difficult to implement consistently in the present VOF framework. Here we provide an alternative approach by increasing the polytropic exponent of the gas after the collapse. This effectively removes internal energy from the bubble and the bubble expansion is reduced. The new polytropic exponent is found by fitting the experimental second re-expansion to the simulation, see solid line in figure 1. Here we use for the polytropic exponent during the initial expansion and collapse $\kappa = 1.4$ and later $\kappa = 2.4$. The increase of κ at the bubble rebound indicates

the energy loss of the bubble at the collapse, e.g. less energy of the bubble is converted to kinetic energy of the flow after its rebound. This energy loss is γ dependent (Vogel & Lauterborn 1988; Vogel *et al.* 1989). By comparing the simulations and experimental results, we find that $\kappa = 2.4$ after the first collapse model sufficiently well the energy loss for $\gamma \approx 1$.

Figure 2 compares the computed bubbles dynamics (left part of each frame) with the experiments (right part of each frame). The rigid boundary for the experiment and the simulation is located at the bottom of each frame. At time $t = 0$ the bubble is nucleated, in the simulation the bubble starts with a spherical nucleus $R(t = 0) = 50 \mu\text{m}$ containing gas at a pressure of $p_g(t = 0) = 1300 \text{ bar}$ while the bright spot in the experiment is due to the plasma emission from the dielectric breakdown. Although the complex plasma and fluid dynamics of the nucleation is ignored already at frame $t = 5 \mu\text{s}$ very good agreement of the expansion dynamics is obtained. After an expansion of the bubble to a maximum volume of an approximate sphere with radius $R(t = 70 \mu\text{s}) = 0.6 \text{ mm}$ the bubble shrinks and develops a jet flow towards the boundary before reaching its minimum volume at $t \approx 135 \mu\text{s}$. During re-expansion a rather complex bubble shape is observed; the bubble separates into a pancake shape close to the boundary and small fragments higher up along the axis of symmetry. The simulations reveal a second splitting at $t = 145 \mu\text{s}$ and re-connection of the flat bottom part when the bubble volume shrinks again, e.g. from $t = 210 \mu\text{s}$. Till the second collapse we find good agreement of the outer shape of the bubble between simulation and experiment; please keep in mind that the simulation shows a cut through the fluid domain while the high-speed recording are a photographic projection of the bubble.

Next we present a comparison of the wall shear stress at one position on the boundary with a measurement of Dijkink & Ohl (2008) for the cavitation bubble at a stand-off $\gamma = 1.0$. For this we have to approximate the wall shear stress as:

$$\tau = \mu \left. \frac{d\mathbf{u}_r}{dy} \right|_{y=0} \approx \mu \left. \frac{\mathbf{u}_r(y)}{y} \right|_{y \leq \epsilon}, \quad (3.1)$$

where \mathbf{u}_r is the flow velocity component parallel to the wall and y is the distance to the boundary, and ϵ is the thickness of the region with constant shear rate which is located within the boundary layer (Schlichting *et al.* 1955; Visser *et al.* 2015). To validate the calculation by equation 3.1, we perform a simulation of the steady submerged wall jet simulation and compare the results with Glauert (1956)'s analytical solution and the classical simulation simulation from Deshpande & Vaishnav (1982), see Appendix. The comparisons indicate that the calculation of the wall shear stress with the present model is reliable once the region with constant shear rate within the boundary layer is resolved.

Before we compare the wall shear stress reproduced by this model to the measurement of Dijkink & Ohl (2008) for the cavitation bubble at a distance of $\gamma = 1.0$, we look for the boundary layer formed by the spreading of the liquid jet induced by collapsing bubble to determine the minimum ϵ . Figure 3(a) shows the vertical distribution of the radial velocity U_x at $t = 133 \mu\text{s}$ and $x = 70 \mu\text{m}$, where the largest shear occurs (see figure 6). The crosses indicate the positions of the resolved cells close to the boundary. We obtain a constant slope over 5 and more cells demonstrating sufficient resolution to resolve the constant shear near the boundary with a thickness of about $1.5 \mu\text{m}$. For $y < 0.4 \mu\text{m}$, U_x is linear with y with a shear rate of 10^8 s^{-1} , i.e. the minimum $\epsilon \approx 0.4 \mu\text{m}$. As a proof that this holds for all the calculations we plot in figure 3(b) the wall shear stress distribution as a function of x using equation 3.1 with $\epsilon = 0.1 \mu\text{m}$ and $\epsilon = 0.2 \mu\text{m}$. The agreement demonstrates that the stresses are fully resolved even for at locations of highest shear. In the remaining calculations we use $\epsilon = 0.1 \mu\text{m}$.

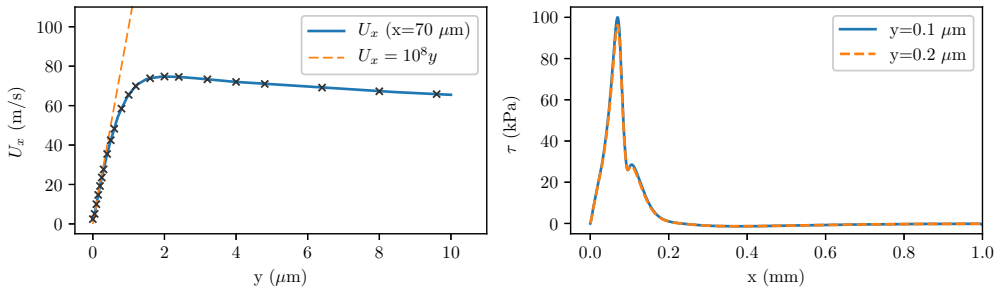


FIGURE 3. Flow and wall shear stress at $t = 133 \mu\text{s}$ for the bubble of $\gamma = 1.0$. (a) the radial velocity distribution along vertical direction within the boundary layer at $x=70 \mu\text{m}$. U_x is linear with a slope of 10^8 when $y < 0.4 \mu\text{m}$; the crosses represent the grid points within the boundary layer. (b) the wall shear stress distribution along boundary calculated at $y = 0.1 \mu\text{m}$ and $y = 0.2 \mu\text{m}$

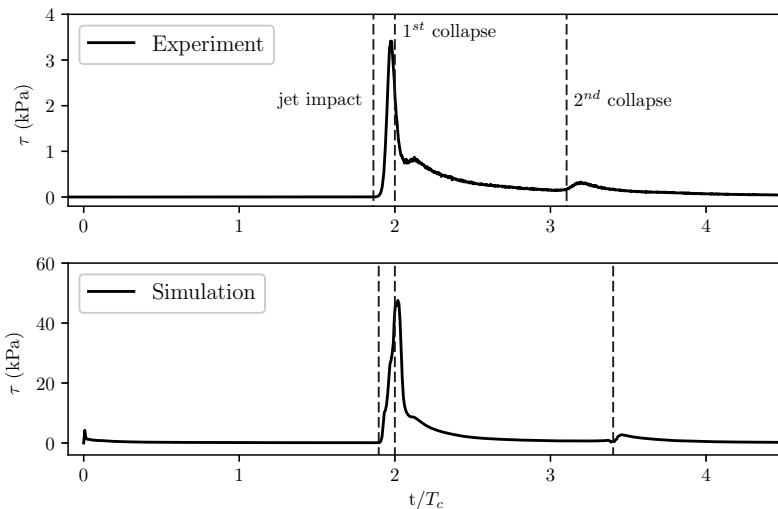


FIGURE 4. Comparison of measured and simulated wall shear stress at a non-dimensional distance of $\eta = 0.33$ from the boundary for the bubble at a distance of $\gamma = 1.0$. The horizontal axis is the dimensionless time normalized by the collapse time T_c , the vertical axis is the wall shear stress in kPa. The dashed lines in each plot represent the instances of jet impact, first collapse, and the second collapse, respectively. The jet impact occurs before the bubble reaches its minimum volume. Also note in experiment $R_{max} \approx 750 \mu\text{m}$, $T_c \approx 80 \mu\text{s}$; in simulation $R_{max} \approx 600 \mu\text{m}$, $T_c \approx 69 \mu\text{s}$. Top: the experimental result from Dijkink & Ohl (2008); Bottom: calculation from current study.

Figure 4 compares the measured and simulated wall shear stresses recorded at $\eta = 0.33$ ($\eta = s/R_{max}$, where s is the distance to the axis of symmetry) at a stand-off parameter of $\gamma = 1.0$. The horizontal axis is the time normalized by the collapse time T_c , while the vertical axis is the measured and calculated wall shear stresses in kPa. In the simulations we have accounted for the imperfections of the stress sensor, i.e. its finite size and non-directivity by taking the average of the absolute of the wall shear stress over the radial distance of $100 \mu\text{m}$. Overall the simulations predict much higher peak wall shear stress than the measurements. We explain this discrepancy with the limited bandwidth of the experimental sensor from Dijkink & Ohl (2008) and the limits of the calibration method

(see below). Let us compare the features qualitatively: the highest value in experiment and simulation is found right after the liquid jet impinges and spreads along the boundary. During the decay of the stress a second peak forms caused by the liquid accelerated by the re-expanding bubble. Moreover the decay of this peak is slow because the flow is stabilized by a vortex ring forming close to the surface. A third peak is also captured in the simulations and found in the measurement. This is due to the re-expansion of the bubble after its second collapse. The features of a prominent peak, a second maximum, slow decay of shear stress during the re-expansion till 2nd collapse, and second peak during 2nd re-expansion are consistently found in experiment and simulation.

3.2. Details of the flow and wall shear stress

We'll now explore the flow within and near the gap formed between the bubble and the rigid boundary. Consecutive snapshots of 6 interesting points in time of the flow ($\gamma = 1.0$, $R_{\max} = 0.6 \text{ mm}$) are shown in Figure 5. The figure depicts the approach of the lower bubble wall towards the rigid boundary during the early bubble expansion ($t = 10 \mu\text{s}$), the early stage of jetting ($t = 130 \mu\text{s}$) and just after jet impact ($t = 133 \mu\text{s}$), then close to minimum volume ($t = 140 \mu\text{s}$) and during the torus collapse ($t = 215 \mu\text{s}$). The last frame in figure 5 shows the early third re-expansion ($t = 245 \mu\text{s}$). Below each frame in figure 5 the wall shear stress is plotted as a function of radial distance in units of 10^3 Pa . Please note that zero crossings of the wall shear stress are stagnation points (or rings). The magnitude of the velocity is color coded. Due to symmetry the origin $x = 0$ remains a stagnation point. At time $t = 10 \mu\text{s}$ the wall shear stress follows the expected shape similar to a source position near an impermeable wall (Ye & Bull 2006). During early collapse the interface closest to the wall flattens into an approximately $50 \mu\text{m}$ thin gap, see $t = 130 \mu\text{s}$. In this gap the shear stress increases with radial distance x and reaches a mild maximum because the radial incoming flow decelerates this gap flow and reflects it upwards. There a stagnation ring is created separating the positive and negative wall shear stresses. Up to this point in time the magnitude of the wall shear stress is comparable with the ones during the spherical bubble expansion, i.e. around 1.0 kPa . A rapid increase of the wall shear stress is seen once the jet pierces with approximately 80 m/s through the lower bubble wall and impacts on the boundary, $t = 133 \mu\text{s}$ in figure 5. The shear stress increases from 0 at the stagnation point to the rim of the jet at $x = 80 \mu\text{m}$ to $\tau \approx 100 \text{ kPa}$. Shortly afterwards at $t = 140 \mu\text{s}$ the spreading jet flow dominates and creates a nearly purely outward directed flow with positive wall shear stresses within the field of view. The maximum τ has shifted downstream with a velocity of 19 m/s . Away from the boundary the jet flow is connected to the expanding flow forming two counter clockwise rotating vortex rings, a large scale encompassing a smaller scale vortex ring. The low pressure at their core stabilizes the expanding bubble fragments into an overall toroidal shaped bubble. The last two frames in figure 5 depict the second collapse and re-expansion at $t = 215 \mu\text{s}$ and $t = 245 \mu\text{s}$, respectively. During collapse we have a similar competition of the flow along the axis of symmetry (however at a much lower velocity than the previous jet flow) with the inward flow due to the bubble acting as a sink. The stagnation ring is now located further away at $x \approx 640 \mu\text{m}$ at $t = 215 \mu\text{s}$. Yet the toroidal bubble fragments into many pieces, which leads to an even more complex flow pattern at $t = 245 \mu\text{s}$.

3.3. Spatio-temporal wall shear stress

Figure 6 provides a detailed view on the spatio-temporal dynamics of the wall shear stress for $\gamma = 1.0$. Positive values of the wall shear stress (directed away from the axis

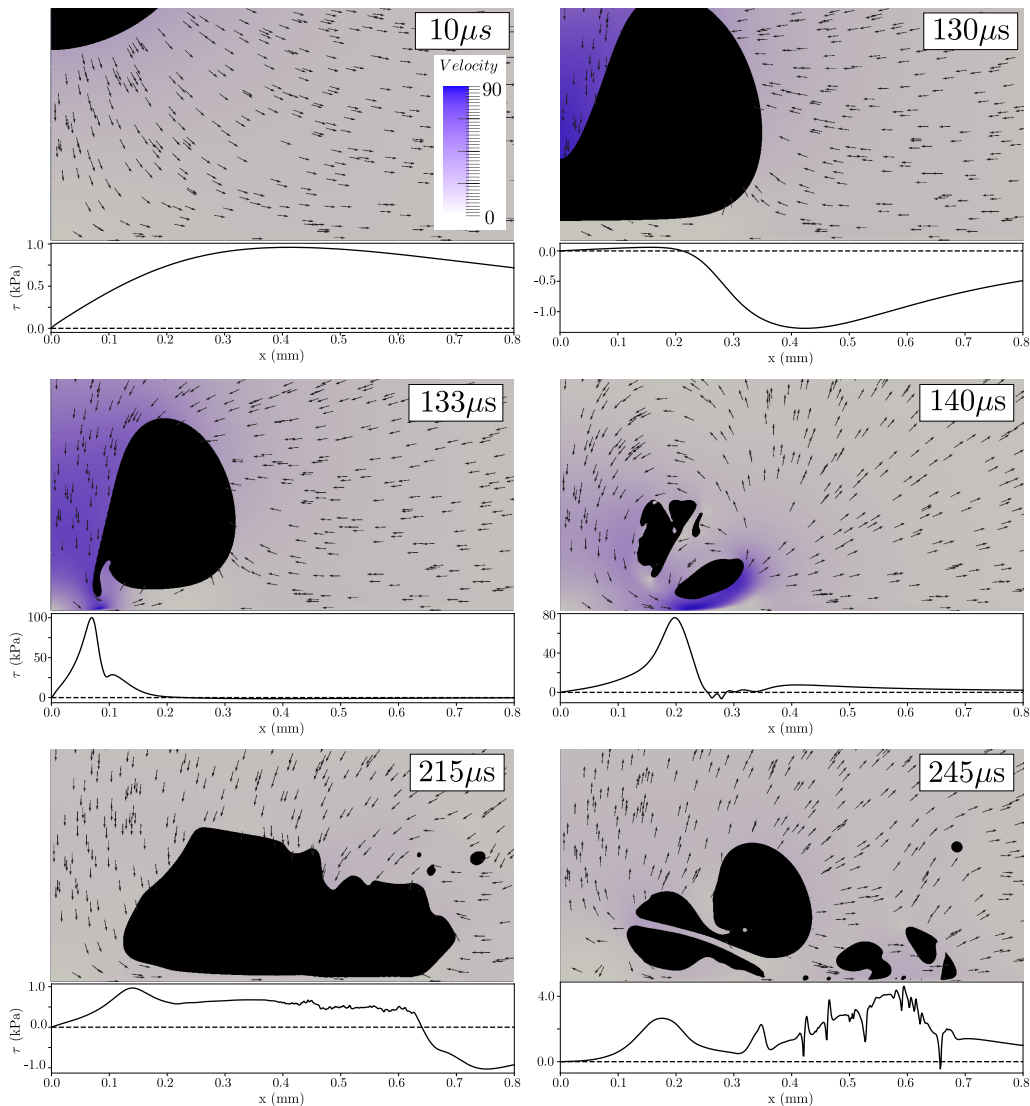


FIGURE 5. Selected flow maps for 6 different times: (a) the early expansion ($t = 10 \mu\text{s}$); (b) during jet formation ($t = 130 \mu\text{s}$); (c) on jet impact ($t = 133 \mu\text{s}$); (d) early re-expansion ($t = 140 \mu\text{s}$); (e) second collapse ($t = 215 \mu\text{s}$); (f) early third expansion ($t = 245 \mu\text{s}$). The plot below the flow fields is the wall shear stress distribution along the radial direction x , the units are μm in along the horizontal and kPa on the vertical axis. Negative values of the wall shear stress depict flow towards the axis of symmetry while positive value in positive radial direction. The velocity is color coded with a unit of m/s.

of symmetry) are plotted in red, while the stress towards $x = 0$ is color-coded in blue. Because of the large range of values the logarithm to the base 10 is taken of the wall shear stress values before plotting. It is evident that the highest stress occurs during the time of first minimum bubble volume $t \approx 135 \mu\text{s}$ near to the axis of symmetry $x \approx 0.15$ mm. During most of the expansion (from $t = 0 \mu\text{s}$ to $t \approx 50 \mu\text{s}$) the stress is positive for the full domain, i.e. when the bubble expands rapidly. However at a later stage of expansion ($t \approx 50 \mu\text{s}$) the stress for large x becomes negative because the expansion is slowed down and the upper bubble wall starts to move towards the boundary driving the liquid at

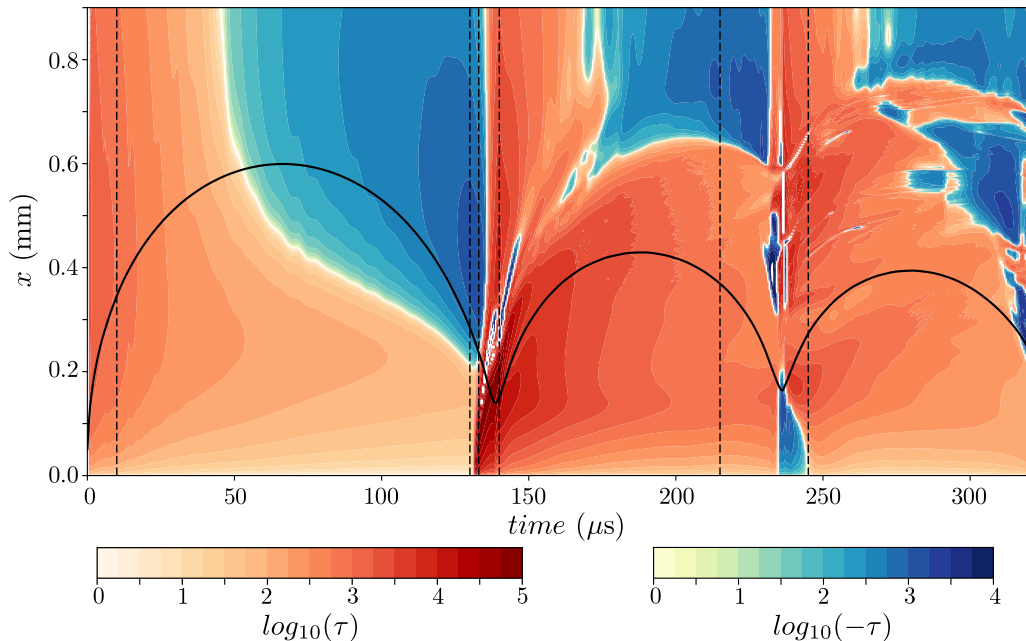


FIGURE 6. The time-space map on the wall shear stress for a standoff distance $\gamma = 1.0$. The first color bar represents the positive wall shear stress (away from the axis of symmetry), while the second one represents the negative wall shear stress. Overlaid is the bubble dynamics as a solid line and the instances shown in figure 5. The unit for τ is Pa.

larger distances inwards. Near the axis of symmetry ($x < 0.2$ mm), the stresses decrease with time but remain positive for the whole expansion and collapse cycle. High stresses occur after $t \approx 132 \mu\text{s}$ in the small x region, this is the instant of time when the liquid jet impacts on the boundary and forms a boundary layer while spreading along the surface. The location of this outward spreading flow is nicely captured in figure 6 by following the location of maximum stress as a function of time. Initially the velocity is about 19 m/s and drops to 1 m/s at $t = 200 \mu\text{s}$. Moreover negative stress is found ahead of the spreading flow (starts from $x \approx 170 \mu\text{m}$ at $t \approx 135 \mu\text{s}$, moves to $x \approx 420 \mu\text{m}$ at $t \approx 146 \mu\text{s}$), which is due to a reversed flow driven by a high adverse pressure gradient. This flow separation is detailed below with figure 7. The stress distribution during the re-expansion and later second collapse of the toroidal bubble differs greatly from the first oscillation cycle. Now a vortex ring has developed which continuously accelerates fluid counter clockwise creating a positive shear stress for the entire second oscillation cycle (also see figure 5 $t = 140 \mu\text{s}$). During the second bubble collapse at time $\approx 240 \mu\text{s}$ the wall shear stress distribution is more complex and the maximum of the shear stress occurs further away from the axis of symmetry ($x \approx 0.45$ mm) due to the toroidal bubble collapse.

Figure 7 shows the boundary flow during the spreading of the impacting liquid jet, from $t = 135 \mu\text{s}$ to $t = 146 \mu\text{s}$. Flow separations and the reversed flow is nicely captured by the streamline and the radial velocity contour. In figure 7, the radial velocity U_x is color coded, the red color represents the flow directed away from the axis of symmetry while blue color indicates the reversed flow (flow to the axis of symmetry). White lines are the streamlines. At $t = 135 \mu\text{s}$, a vortex ring is nucleated at $x \approx 180 \mu\text{m}$ due to an adverse pressure caused by the fast flow spreading over the stagnant liquid. As a result the flow close to the boundary is opposite to the main flow resulting in a shear stress

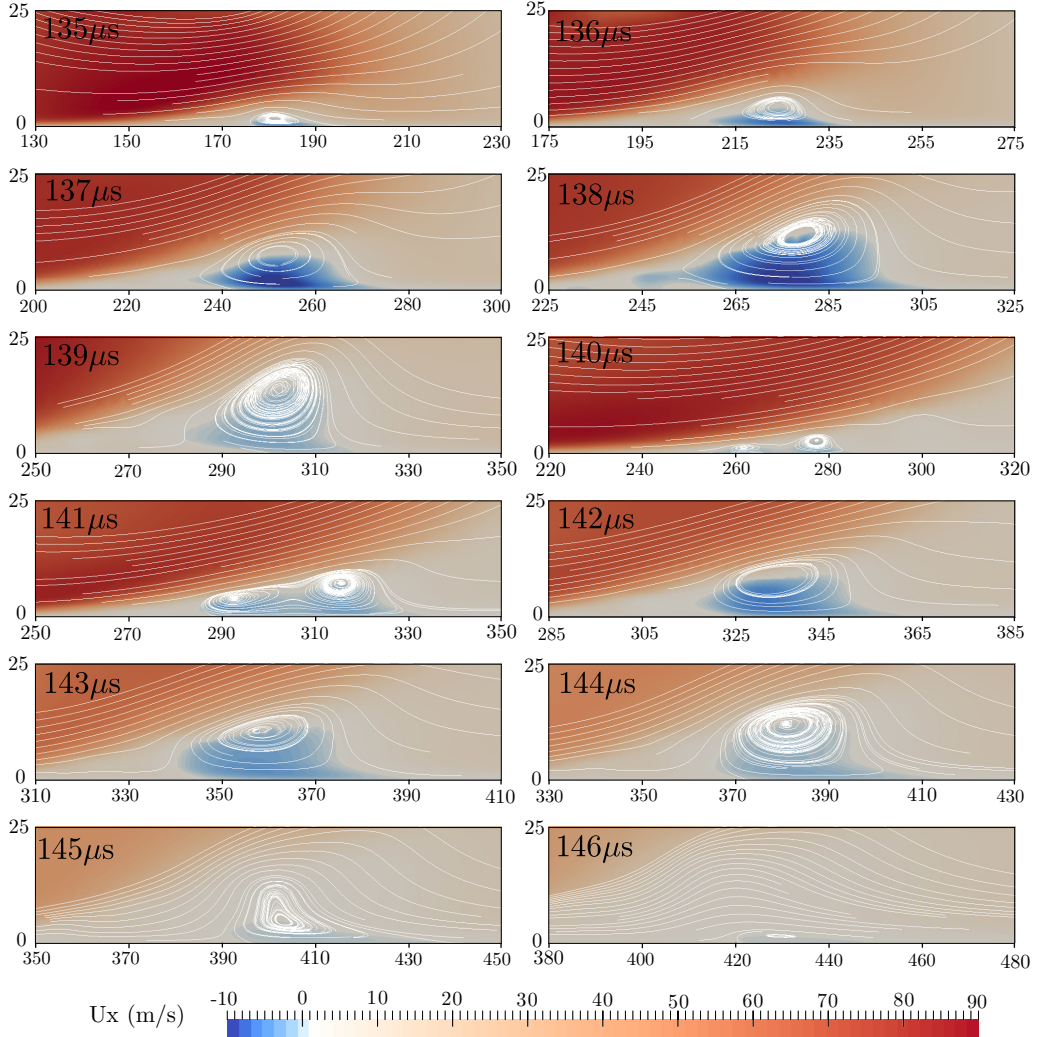


FIGURE 7. Flow separations during the jet spreading and bubble re-expansion. The radial velocity U_x is color coded, the blue color indicates the reversed flow (flow to the axis of symmetry); white line represents the streamline; the spatial units are in μm . Please note that the offset of the x-axis differs in the frames.

direction opposite to the driving jet flow. The vortex ring expands in size and moves outwards with a velocity of around 25 m/s between $t = 135 \mu\text{s}$ to $t = 138 \mu\text{s}$ inducing a maximum negative velocity at $t = 138 \mu\text{s}$ of 10 m/s before it slows down at $t = 139 \mu\text{s}$. The flow from the re-expanding bubble triggers two new vortex rings at $t = 141 \mu\text{s}$ which coalesce into a single ring at $t = 142 \mu\text{s}$ and is transported with a velocity of approx. 20 m/s before it decays at $t = 146 \mu\text{s}$.

4. Discussions and Conclusion

The present simulations predict a complex spatiotemporal distribution of the wall shear stress during the non-spherical collapse of a bubble near a rigid wall. We have compared the temporal dynamics of the amplitude on the wall and found qualitative agreement

with measurements. In particular that a short lived stress of maximum amplitude is generated just after impact and during the early spreading of the jet, while a vortex ring which is formed during the re-expansion contributes for a longer duration stress at a lower amplitude. The simulations predict stresses of the order of 50 kPa while the experimental results are an order of magnitude lower. The difference may be explained with the calibrations conducted for the shear stress measurements. These were conducted over a range from 0.05 Pa to 10 Pa (Dijkink & Ohl 2008). Maisonhaute *et al.* (2002b) provided a rough yet considerably higher estimate based on their earlier electrochemical measurements of the flow velocity of around 200 m/s at the distance of 40 to 80 nm to the boundary (Maisonhaute *et al.* 2002a). They predict that shear stress from oscillating and jetting bubbles driven by ultrasound could provide 25 – 50 bar. In contrast bubbles oscillating only mildly with no or little deformation of their shape may create shear stresses of the order of a few kPa, according to simulations from Krasovitski & Kimmel (2004).

Chahine *et al.* (2016) have simulated the (inviscid) collapse of a bubble near a movable dirt particle with a focus of the forces generated by the pressure drag on the particle. Already during expansion of the bubble the particle may be pushed along the surface, while the complex recirculating flow after the bubble collapse may attract or push away the particle depending on the specific configuration. However to understand the particle dynamics better, a more complex fluid-structure-interaction model should be included.

The importance of the flow following the collapse of the bubble has also been acknowledged in the experimental study by Reuter & Mettin (2016). There the strongest cleaning effect was observed for $\gamma \leq 1.1$ and was explained with the interaction of the jet spreading flow with the inward flow during the collapse. This results in a wall bound vortex creating a long lasting exposure of the surface to shear. The present simulations confirm this scenario and are revealing the complex interaction leading to multiple stagnation rings and opposing directions of the shear stress.

Already during the expansion and early collapse of the bubble, the shear stresses are of the order of 1 kPa while their increase to around 100 kPa occurs after the liquid jet impact; a system of vortex ring is formed under the combined effect of the main shear flow and the re-expansion of the toroidal bubble, which stabilizes the flow and thereby slows down the decay of the shear stress.

Starting from the present results it will be interesting to conduct a detailed parameter study to evaluate the effect of bubble size, viscosity, and density. For example, in ultrasound cleaning baths smaller bubbles are found which may not generate strong re-entrant jets (Kim & Kim 2014) yet they translate along the surface (Kim *et al.* 2009; Zijlstra *et al.* 2009). Simulations with suitable measurement techniques, which may still have to be developed, will help to understand how bubbles clean.

Appendix A. Determination of the Wall Shear Stress

To validate the calculation of wall shear stress from the code, we now reproduce the steady wall jet impingement simulation by Deshpande & Vaishnav (1982): a cylindrical submerged jet impacting on to a no-slip flat surface. The jet is with a radius of $R_{jet} = 50 \mu\text{m}$ and a flat velocity of U_{jet} , whose inlet is located $d = 4R_{jet} = 200 \mu\text{m}$ above the boundary. The domain is axisymmetric with both width and height of $10R_{jet}$. The mesh is with a spacing $\Delta x = 2.5 \mu\text{m}$ in the bulk flow while is refined to $\Delta x = 0.05 \mu\text{m}$ in the near boundary region. Glauert (1956) gave an analytic similarity solution of the wall shear stress for this problem:

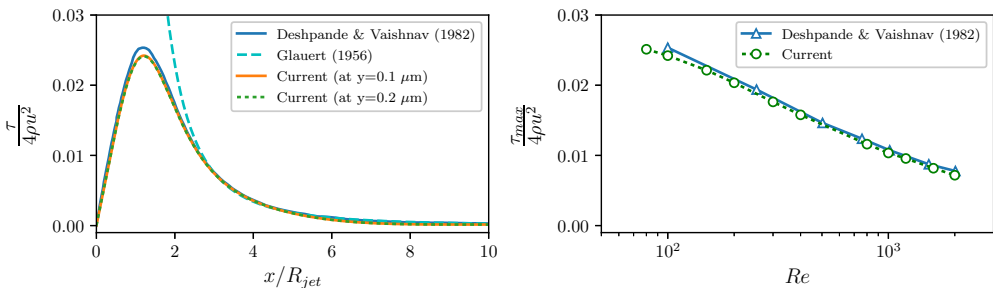


FIGURE 8. Comparison on wall shear stress of the submerged jet impingement. (a) the normalized stress distribution on wall for $Re = 100$; the blue line is the result of Deshpande & Vaishnav (1982), the orange line and green dotted line represent the result calculated at $y = 0.1 \mu m$ and $y = 0.2 \mu m$ from the simulation, while the cyan dash line is the Glauert solution. (b) the maximum normalized wall shear stress of various Re Number from Deshpande & Vaishnav (1982) and the current simulations.

$$\tau = \mu \left. \frac{d\mathbf{u}_r}{dy} \right|_{y=0} = \rho \left(\frac{125F^3\rho}{216\mu x^{11}} \right)^{1/4}, \quad (\text{A } 1)$$

where ρ is the flow density and F the momentum flux which is defined as $F = (1/8)U_{jet}^3 R_{jet}^4$ for a jet with a flat velocity profile.

Figure 8(a) shows the comparison on the wall shear stress distribution along the boundary of our current calculation and the numerical result of Deshpande & Vaishnav (1982) and the Glauert solution (equation A 1) for the case $Re = 100$, where $Re = 2\rho U_{jet} R_{jet}/\mu$ is the defined Reynolds number. The current calculation of the wall shear stress from equation 3.1 at $y = 0.1 \mu m$ and $y = 0.2 \mu m$ is indistinguishable, indicating that the stress is converged in the near boundary cells and the flow field in the region with constant shear rate is resolved. The stress distribution along the boundary from the current simulation matches very well with Deshpande & Vaishnav (1982) as well as the Glauert solution for $x/R_{jet} > 3$. The normalized maximum shear stress $\tau_{max}/(4\rho U_{jet}^2)$ is also compared to the numerical work of Deshpande & Vaishnav (1982, 1983), good agreement is found for a wide Re numbers. Thus the calculation of the wall shear stress using our current model is reliable once the region with constant shear rate in the boundary layer is determined.

We acknowledge financial support from the Office of Naval Research under Grant No. N62909-16-1-2139. We further thank anonymous referees for their helpful suggestions to improve the manuscript.

REFERENCES

- BEST, JP & KUCERA, A 1992 A numerical investigation of non-spherical rebounding bubbles. *Journal of fluid mechanics* **245**, 137–154.
- BLAKE, JOHN R & GIBSON, DC 1987 Cavitation bubbles near boundaries. *Annual review of fluid mechanics* **19** (1), 99–123.
- BRACKBILL, JU, KOTHE, DOUGLAS B & ZEMACH, CHARLES 1992 A continuum method for modeling surface tension. *Journal of computational physics* **100** (2), 335–354.
- CHAHINE, GEORGES L, KAPALI, ANIL, CHOI, JIN-KEUN & HSIAO, CHAO-TSUNG 2016 Modeling of surface cleaning by cavitation bubble dynamics and collapse. *Ultrasonics sonochemistry* **29**, 528–549.

- COLE, ROBERT HUGH 1965 *Underwater explosions*. Dover Publications.
- DESHPANDE, MOHAN D & VAISHNAV, RAMESH N 1982 Submerged laminar jet impingement on a plane. *Journal of Fluid Mechanics* **114**, 213–236.
- DESHPANDE, MOHAN D & VAISHNAV, RAMESH N 1983 Wall stress distribution due to jet impingement. *Journal of Engineering Mechanics* **109** (2), 479–493.
- DIJKINK, RORY & OHL, CLAUS-DIETER 2008 Measurement of cavitation induced wall shear stress. *Applied Physics Letters* **93** (25), 254107.
- GLAUERT, MB 1956 The wall jet. *Journal of Fluid Mechanics* **1** (6), 625–643.
- GONZALEZ-AVILA, S ROBERTO, HUANG, XIAOHU, QUINTO-SU, PEDRO A, WU, TOM & OHL, CLAUS-DIETER 2011 Motion of micrometer sized spherical particles exposed to a transient radial flow: attraction, repulsion, and rotation. *Physical review letters* **107** (7), 074503.
- KIM, TAE-HONG & KIM, HO-YOUNG 2014 Disruptive bubble behaviour leading to microstructure damage in an ultrasonic field. *Journal of Fluid Mechanics* **750**, 355–371.
- KIM, WONJUNG, KIM, TAE-HONG, CHOI, JAEHYUCK & KIM, HO-YOUNG 2009 Mechanism of particle removal by megasonic waves. *Applied Physics Letters* **94** (8), 081908.
- KOCH, MAX, LECHNER, CHRISTIANE, REUTER, FABIAN, KÖHLER, KARSTEN, METTIN, ROBERT & LAUTERBORN, WERNER 2016 Numerical modeling of laser generated cavitation bubbles with the finite volume and volume of fluid method, using openfoam. *Computers & Fluids* **126**, 71–90.
- KOUKOUVINIS, P, GAVAISES, M, SUPPONEN, O & FARHAT, M 2016a Numerical simulation of a collapsing bubble subject to gravity. *Physics of Fluids* **28** (3), 032110.
- KOUKOUVINIS, P, GAVAISES, M, SUPPONEN, O & FARHAT, M 2016b Simulation of bubble expansion and collapse in the vicinity of a free surface. *Physics of Fluids* **28** (5), 052103.
- KRASOVITSKI, BORIS & KIMMEL, EITAN 2004 Shear stress induced by a gas bubble pulsating in an ultrasonic field near a wall. *IEEE transactions on ultrasonics, ferroelectrics, and frequency control* **51** (8), 973–979.
- LE GAC, SÉVERINE, ZWAAN, ED, VAN DEN BERG, ALBERT & OHL, CLAUS-DIETER 2007 Sonoporation of suspension cells with a single cavitation bubble in a microfluidic confinement. *Lab on a Chip* **7** (12), 1666–1672.
- LEE, M, KLASEBOER, E & KHOO, BC 2007 On the boundary integral method for the rebounding bubble. *Journal of Fluid Mechanics* **570**, 407–429.
- MACDONALD, J ROSS 1969 Review of some experimental and analytical equations of state. *Reviews of Modern Physics* **41** (2), 316.
- MAISONHAUTE, EMMANUEL, BROOKES, BENJAMIN A & COMPTON, RICHARD G 2002a Surface acoustic cavitation understood via nanosecond electrochemistry. 2. the motion of acoustic bubbles. *The Journal of Physical Chemistry B* **106** (12), 3166–3172.
- MAISONHAUTE, EMMANUEL, PRADO, CESAR, WHITE, PAUL C & COMPTON, RICHARD G 2002b Surface acoustic cavitation understood via nanosecond electrochemistry. part iii: Shear stress in ultrasonic cleaning. *Ultrasonics sonochemistry* **9** (6), 297–303.
- MILLER, ST, JASAK, HRVOJE, BOGER, DA, PATERSON, EG & NEDUNGADI, A 2013 A pressure-based, compressible, two-phase flow finite volume method for underwater explosions. *Computers & Fluids* **87**, 132–143.
- NARAYANAN, V, SEYED-YAGOOBI, J & PAGE, RH 2004 An experimental study of fluid mechanics and heat transfer in an impinging slot jet flow. *International Journal of Heat and Mass Transfer* **47** (8), 1827–1845.
- OHL, CLAUS-DIETER, ARORA, MANISH, DIJKINK, RORY, JANVE, VAIBHAV & LOHSE, DETLEF 2006a Surface cleaning from laser-induced cavitation bubbles. *Applied physics letters* **89** (7), 074102.
- OHL, CLAUS-DIETER, ARORA, MANISH, IKINK, ROY, DE JONG, NICO, VERSLUIS, MICHEL, DELIUS, MICHAEL & LOHSE, DETLEF 2006b Sonoporation from jetting cavitation bubbles. *Biophysical journal* **91** (11), 4285–4295.
- PHARES, DENIS J, SMEDLEY, GREGORY T & FLAGAN, RICHARD C 2000 The wall shear stress produced by the normal impingement of a jet on a flat surface. *Journal of Fluid Mechanics* **418**, 351–375.
- REUTER, FABIAN & METTIN, ROBERT 2016 Mechanisms of single bubble cleaning. *Ultrasonics sonochemistry* **29**, 550–562.

- RUSCHE, HENRIK 2003 Computational fluid dynamics of dispersed two-phase flows at high phase fractions. PhD thesis, Imperial College London (University of London).
- SCHLICHTING, HERMANN, GERSTEN, KLAUS, KRAUSE, EGON & OERTEL, HERBERT 1955 *Boundary-layer theory*, , vol. 7. Springer.
- VISSER, CLAAS WILLEM, GIELEN, MARISE V, HAO, ZHENXIA, LE GAC, SÉVERINE, LOHSE, DETLEF & SUN, CHAO 2015 Quantifying cell adhesion through impingement of a controlled microjet. *Biophysical journal* **108** (1), 23–31.
- VOGEL, A & LAUTERBORN, W 1988 Acoustic transient generation by laser-produced cavitation bubbles near solid boundaries. *The Journal of the Acoustical Society of America* **84** (2), 719–731.
- VOGEL, A, LAUTERBORN, W & TIMM, R 1989 Optical and acoustic investigations of the dynamics of laser-produced cavitation bubbles near a solid boundary. *Journal of Fluid Mechanics* **206**, 299–338.
- WANG, QIANXI 2014 Multi-oscillations of a bubble in a compressible liquid near a rigid boundary. *Journal of Fluid Mechanics* **745**, 509–536.
- WELLER, HENRY G, TABOR, G, JASAK, HRVOJE & FUREBY, C 1998 A tensorial approach to computational continuum mechanics using object-oriented techniques. *Computers in physics* **12** (6), 620–631.
- YE, TAO & BULL, JOSEPH L 2006 Microbubble expansion in a flexible tube. *Journal of biomechanical engineering* **128** (4), 554–563.
- ZIJLSTRA, AALDERT, JANSSENS, TOM, WOSTYN, KURT, VERSLUIS, MICHEL, MERTENS, PAUL W & LOHSE, DETLEF 2009 High speed imaging of 1 mhz driven microbubbles in contact with a rigid wall. In *Solid State Phenomena*, , vol. 145, pp. 7–10. Trans Tech Publ.